Porosity evolution in proton irradiated microfine-grained POCO graphite

Ming Jiang [1], Kavin Ammigan[2], George Lolov[2], Frederique Pellemoine[2] and Dong Liu[1*]

[1] HH Wills Physics Laboratory, School of Physics, University of Bristol, Bristol, BS8 1TL, UK

[2] Target Systems Department, Fermi National Accelerator Laboratory, Batavia IL 60510-5011, USA

[*]Contact: dong.liu@bristol.ac.uk

Abstract

This work investigated the porosity evolution of POCO ZXF-5Q graphite that has been irradiated by 340 kW, 120 GeV protons inside NT02 target system in Fermilab's NuMI beamline. This POCO graphite has undergone direct bulk dimensional swelling at low dose irradiation and its local microstructural change is still not well-understood during this process. In this work, the (sub-) micrometre scale porosity from six locations across proton beam fluence and temperature gradients have been studied using focused ion beam-scanning electron microscopy (FIB-SEM) tomography. A deep learning-based tomographic image segmentation technique has been established and implemented for porosity segmentation and quantification. It has been found that there is a decrease in the total volumetric percentage of the porosity at proton beam centre (~ 8 - 8.4 vol.%), by comparing to un-irradiated POCO (~ 12 - 13 vol.%) and to beam 2σ and 5σ radii (~ 12 vol.%). This decrease in porosity volume percentage was found to be caused by the reduction in pores with volumes > 0.1 μm^3 induced by material bulk dimensional swelling at proton beam centre area. The porosity reduction in relation to dimensional change and irradiation creep was discussed and further investigations through well-controlled irradiation experiment are still needed.

1. Introduction

Fine-grained graphite is used as a particle production target material at major particle accelerator facilities around the world. High-energy high-intensity proton beams are directed

onto graphite target material to produce secondary particles which further decay into muons or neutrinos for high-energy physics experiments[1-4]. And this is exemplified by the future Deep Underground Neutrino Experiment (DUNE), an international particle physics experiment led by the U.S. Fermi National Accelerator Laboratory (Fermilab). The neutrinos for this experiment will be produced by the Fermilab Long Baseline Neutrino Facility (LBNF), a multi-megawatt (MW) accelerator target facility. In searching for suitable candidate target graphite materials, several irradiation experiments and studies have been conducted. Past experience in using target POCO ZXF-5Q graphite for the MINOS/MINERvA experiments at Fermilab has shown a decline of neutrino yield during the target's lifetime and eventual target failure was observed by crack formation along the target fins. It is therefore of great importance to understand irradiation behaviour and microstructural changes of fine-grained graphite under pulsed and high-energy (120 GeV) high-intensity proton irradiation, to help optimise the selection and design of future target systems for next generation MW-class proton accelerators. Further to these, POCO ZXF-5Q graphite is also considered to be a surface sealing material for nuclear graphite component in molten salt reactors (MSR) owing to its superior resistance to molten salt infiltration and gas permeation benefiting from its much finer porosity[5,6] while allowing for the transport and removal of ^{135}Xe[6-9].

Nuclear graphite inevitably possesses a variety of microstructural phases spanning across several length-scales due to its raw material and manufacturing process used, with porosity being one of the predominant type of defects distributed through the entire material volume[10-14]. The origin and morphological characteristics of different types of pores in nuclear graphite have attracted great research interest due to their important role in affecting crystal/bulk dimensional changes as well as physical and thermo-mechanical property changes with irradiation and temperature[15-19,20-24]. The most well-known nuclear graphite dimensional change behaviour is an initial bulk volumetric shrinkage followed by swelling back to its original bulk volume, the so-termed 'turn-around' behaviour. The initial shrinkage was attributed to the closure of pre-existing porosity in the form of microcracks (Mrozowski type cracks) upon irradiation and thermal straining[13]. The mechanical properties of nuclear graphite, such as elastic modulus and strength also change with irradiation showing an initial increase due to both dislocation pinning by interstitials[25,26] and crystal densification process[20,27]. The 'turn-around' point is usually at ~ 18 dpa for near-isotropic Gilsocarbon graphite at

430 °C[28]. It is generally believed that the bulk volumetric swelling starts when nano-scale accommodating cracks are filled; the newly created microstructural defects will coalesce and grow to a critical size eventually leading to the structural disintegration of graphite at high doses.

There is also evidence from the modelling results by Hall *et al.*[29] demonstrating that c-axis expansion could be accommodated by closure of large lenticular cracks (at hundred micrometre scale) within in Gilsocarbon graphite filler particles, contributing to the bulk dimensional change and affecting the 'turn-around' behaviour of nuclear graphite (and hence, termed 'accommodation porosity'). Faster 'turn-around' at higher irradiation temperature was attributed to more accommodation porosity being taken up by thermal expansion in their work. Haag[30] showed micrographs depicting Gilsocarbon graphite bulk volume and filler particle shrinkage with most of the filler macro-porosity being closed at bulk dimensional shrinkage stage. However, microfine-grained POCO graphite, along with other grades of medium-/ fine-grained graphites, exhibited direct bulk dimensional swelling at doses even lower than 1 dpa across a range of temperatures[31-36]. There is not yet a satisfactory mechanism established for explaining this initial swelling. It is also not clear if the mechanism that is responsible for the bulk dimensional swelling beyond 'turn-around' at high doses is also contributing to POCO graphite initial bulk dimensional swelling at low dose. This will be further discussed in the Discussion section.

Nuclear graphite can also be subjected to thermal and radiolytic oxidation-induced structural and property changes within CO_2-cooled, graphite moderated thermal fission reactors[23,28,37,38]. Whilst thermal oxidation is negligible in Magnox and UK advanced gas-cooled reactors (AGRs), radiolytic oxidation considerably modifies open pores in nuclear graphite. It is generally accepted that open pores serve as favourable reaction sites for radiolytic oxidising species to react with carbon atoms causing loss of graphite weight and decrease in density, with smaller pore being more susceptible to such process[39]. Graphite density, modulus and strength would be further degraded with more pores enlarged and generated. Although radiolytic oxidation is not of an issue in high temperature gas-cooled reactors (HTGRs), very high temperature reactors (VHTRs) and MSR due to the different coolant media, which are inert helium and molten salt[9], chronic thermal oxidation could still happen in HTGRs and VHTRs under high temperatures (>600°C), as a result of potential introduction of oxidising

impurities carried by helium circulation during normal operation, and significant oxidation due to air/water ingress under accident conditions[9,40,41]. For neutrino-production targets at Fermilab's NT02 target system, oxidation is currently not of primary concern because of the inert He environment inside the target system and relatively low service temperature currently at ~370 °C (peak temperature). But the possibility of oxidising agent such as air and other impurities being introduced into the target system is not excluded in case of accident such as casing and cooling pipe breaks. This would pose a serious graphite oxidisation issue under such circumstances via in-pore diffusion controlled manner, especially when operating at elevated temperatures (> 670 °C) in Fermilab's NOvA experiment, future LBNF-DUNE experiment, and 737 °C in the T2K experiment[42]. Considering POCO ZXF-5Q graphite contains predominantly (sub-) micrometre sized (< 1μm) porosity of which 70-95 % are open pores[12,43,44], it is therefore necessary to characterise its porosity evolution with service for oxidation considerations.

This work investigates the porous microstructure across fluence and temperature gradients in a piece of ex-service POCO ZXF-5Q graphite material extracted from the NT02 target system in Fermilab's NuMI beamline (hence termed NT02 POCO). (Sub-) micrometre scale 3D porosity structures from three locations with different irradiation damage levels are studied by FIB-SEM tomography. The datasets are post-processed and corrected in Avizo software. Porosities are segmented by deep learning methodology in ORS Dragonfly software[45] to demonstrate the feasibility and the first implementation of such technique in irradiated POCO graphite structural characterisation in open literature. Thorough porosity analysis has been carried out to closely examine the evolution of the pore structures with proton irradiation.

2. Materials and Methods

2.1 Materials

The material studied in this work is a proton irradiated microfine-grained POCO ZXF-5Q graphite, manufactured by Entegris - POCO Materials (former POCO Graphite Inc), USA. It has a reported average grain size of 1 μm and ~20% nominal total porosity. Its basic physical

and mechanical properties have been reported elsewhere[44,46]. The NT02 target system design at Fermilab's NuMI beamline and irradiation condition has also been well-documented in these references[31,47].

POCO ZXF-5Q graphite is remarkably different from conventional nuclear grades of graphite such as PGA and Gilsocarbon and other fine-grained graphite such as IG-110 and Mersen 2020 in terms of porosity. From the work by Arregui-Mena *et al.*[12] and Jiang *et al.*[44], it has been found that: 1) POCO ZXF-5Q graphite consists of mainly irregularly shaped globular pores with strong interconnectivity, closely resembling gas run pores that could be found in conventional nuclear graphite. 2) The size of porosity in POCO ZXF-5Q graphite is in general smaller than most of the fine-grained graphite grades examined, such as IG-110, NBG-25 and ETU-10 evidenced by mercury porosimetry, and SGL R7650 and IG-430 by 3D image-based analysis. 3) POCO ZXF-5Q graphite porosity is uniformly distributed across its bulk volume with a relatively large porosity volumetric percentage (> 20 vol.%).

Additionally, POCO ZXF-5Q graphite is considered as a binderless graphite material[48]. Although the exact manufacturing route and raw materials used as filler and binder material for production are not disclosed by its manufacturer, it has been confirmed by Pitner that a similar grade, POCO AXF, does not seem to have continuous binder phase with no clear filler-binder boundaries can be seen[36]. Another POCO grade AXM-5Q1 is also claimed not to have any binder materials[48]. Further, Campbell mentioned that POCO ZXF-5Q graphite is produced in a way similar to sintering for producing ceramics that fine-grained filler powders are directly isostatically compressed together to form green article without using any binder material[49]. It has been recently confirmed that no binder materials and filler-binder interface can be seen in POCO ZXF-5Q by μXCT and FIB-SEM tomography by Jiang *et al*[44]. These findings indicate that POCO ZXF-5Q graphite comprises only filler grains and porosity and the origin of the micrometre scale porosity in POCO ZXF-5Q graphite is different to those gas-percolation pores in other nuclear graphite grades resulted from release of volatiles from binder material during baking stage.

2.2 Focused ion beam-scanning electron microscopy (FIB-SEM) tomography

To examine POCO graphite's local porosity at sub-micrometre scale, after high-energy proton irradiation, FIB-SEM tomography using a FEI Helios NanoLab 600i dualbeam workstation at Materials Research Facility (MRF) of UK Atomic Energy Authority (UKAEA) has been conducted on the fractured surface of the NT02 POCO fin at proton beam centre (origin), 2σ and 5σ distance from beam centre, Fig 1. The specimen has been oriented in such a way that its fractured surface is facing upwards so that the stitched SEM image in Fig 1b is a top-down view, and proton beam is travelling into/out of paper's direction with its centre being marked by red dot. Two FIB-SEM tomographies have been performed at each of these locations to give higher statistical confidence.
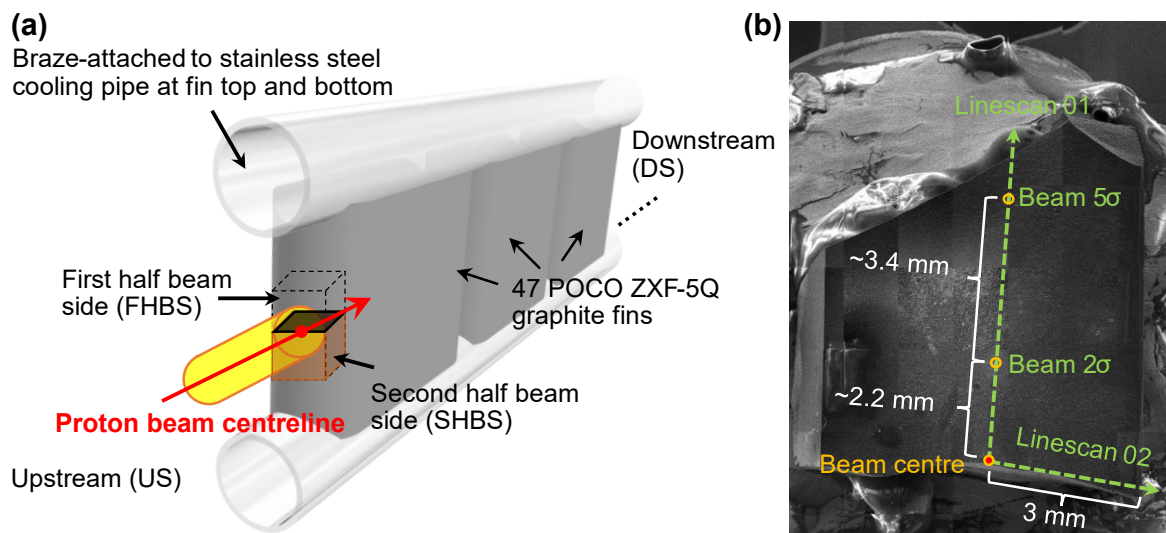
Fig 1. Schematic showing POCO ZXF-5Q graphite specimen extracted from the NuMI beamline of Fermilab. (a) The NT0-2 target system employed at NuMI beamline consists an array of 47 segmented fins of POCO ZXF-5Q graphite with their top and bottom surfaces being braze-attached to stainless-steel cooling pipe containing circulating water for heat removal. False colours are for eye guidance only. (b) Stitched SEM micrograph showing the extracted piece of specimen located close to proton beam centre, which is called second half beam side (SHBS) in (a). This specimen has been re-oriented to expose its internal fractured surface for examination and therefore, proton beam travelling direction in (b) is perpendicular to paper. Beam 1σ radius = 1.1 mm. FIB-SEM tomographies have been conducted at 3 locations on the fractured surface: beam centre, beam 2σ radius and beam 5σ radius. Linescan01 and Linescan02 directions shown here are two perpendicular directions along sample fractured surface for reference.

All FIB-SEM tomographies followed the same procedure: 1) A protective Pt layer is deposited onto the surface of region of interest (ROI) chosen; 2) trenches are milled by Ga^+ beam at 30 kV and 47 nA in front of and at both sides of the ROI; 3) Ga^+ beam at 30 kV 9.3 nA was used for cleaning cross section and the whole milling process for all sites. SEM at 10 kV and 0.34 nA was used for all imaging. Automated electron beam shift in Y direction (milling progressing direction) has been enabled in three of the tomographies to correct for shearing artefact and keeping tracking focus. Automated milling and imaging were performed by using the FEI software Auto Slice and View G3. Post-mortem instrument artefact correction and tomography image processing followed the procedures described in these references[50-53]. Specifically, Avizo Standard 9.7.0 (ThermoFisher Scientific, USA) was used for foreshortening correction, image alignment by least-squares algorithm, denoising and curtaining artefact removal by non-local means filter and eventually shading correction. Tomography datasets without electron beam Y shift correction have been further corrected for shearing artefact in Avizo. Relevant information including tomography settings, dataset voxel size, correction and reconstruction steps are summarised in Table 1.

Corrected FIB-SEM tomography datasets were then taken to deep-learning segmentation by using ORS Dragonfly software (Object Research Systems, Canada) to separate porosity from solid phases. Application of the same commercial deep learning environment to the segmentation of SiC-SiC matrix composite X-ray tomography data has been documented[54]. To initially train the deep learning models, about 10 tomography slices were manually segmented for each of these datasets separating porosity from solid phase. Dragonfly's built-in models including Sensor 3D[55], 2D U-Net model[56], 3D U-Net model[56] and FC-DenseNet56[57] were selected for initial training and comparing performances with identical training parameters setup. All of these models scored over 0.96 after this first round of training with 2D U-Net model surpassed the others in all 6 datasets. Their performance at this stage was further judged by closer visual inspection of prediction segmentations made. This has led to the final decision that the convolutional 2D U-Net model with depth level 4 and initial filter count 64 (2D U-Net_dl-4_ifc-64 model) is kept, with the remaining models subsequently abandoned. This kept 2D U-Net_dl-4_ifc-64 model was then used for predicting more slices that were later back-fed into the model for further training session. Eventually the 2D U-Net_dl-4_ifc-64 model scored over ~0.997 after been trained with a total number of 20-25 slices

(~4-5% of each dataset) depending on the specific dataset. A flow chart is drawn to schematically show this process in Fig 2. Key deep learning model training parameters are summarised in Table 2.

210　*Table 1. FIB-SEM tomography setup and dataset post-processing parameters.*

|	Beam centre		Beam 2σ (~2200 μm from centre)		Beam 5σ (~5600 μm from centre)	
	Site 1	Site 2	Site 1	Site 2	Site 1	Site 2
Pt layer size (μm³)	25×25×1.5	22×22×2	20×22×1.2	30×30×2.5	20×22×1.2	25×25×2.5
Approx. volume milled (μm³)	27×20×25	23×22×25	26×18×22	30×30×25	30×18×23	27×32×20
Voxel size (μm³)	0.04×0.04×0.05	0.025×0.025×0.05	0.04×0.04×0.05	0.027×0.027×0.05	0.04×0.04×0.05	0.037×0.037×0.05
Pt deposition current and voltage	30 kV, 0.79 nA	30 kV, 2.5 nA	30 kV, 0.79 nA	30 kV, 2.5 nA	30 kV, 0.79 nA	30 kV, 2.5 nA
Trenching voltage and current	30 kV, 9.3 nA	30 kV, 47 nA and 21 nA	30 kV, 9.3 nA	30 kV, 47 nA and 21 nA	30 kV, 9.3 nA	30 kV, 47 nA and 21 nA
Cleaning cross-section voltage and current	30 kV, 6.5 nA and 9.3 nA					
Milling and slicing voltage and current	30 kV, 9.3 nA					
SEM imaging voltage and current	Secondary electron (SE), 10 kV, 0.34 nA					
Final dataset dimension after correction and cropping (voxels)	551×293×490	904×499×500	561×301×440	891×531×496	696×351×460	701×421×335
Corrected voxel size (μm³)	0.04×0.05×0.05	0.025×0.032×0.05	0.04×0.05×0.05	0.027×0.034×0.05	0.04×0.05×0.05	0.037×0.047×0.05
Final dataset physical size after correction and cropping (μm³)	22×14.7×24.5	22.6×16.0×25	22.4×15.1×22	24.1×18.1×24.8	27.8×17.6×23	25.9×19.8×16.8
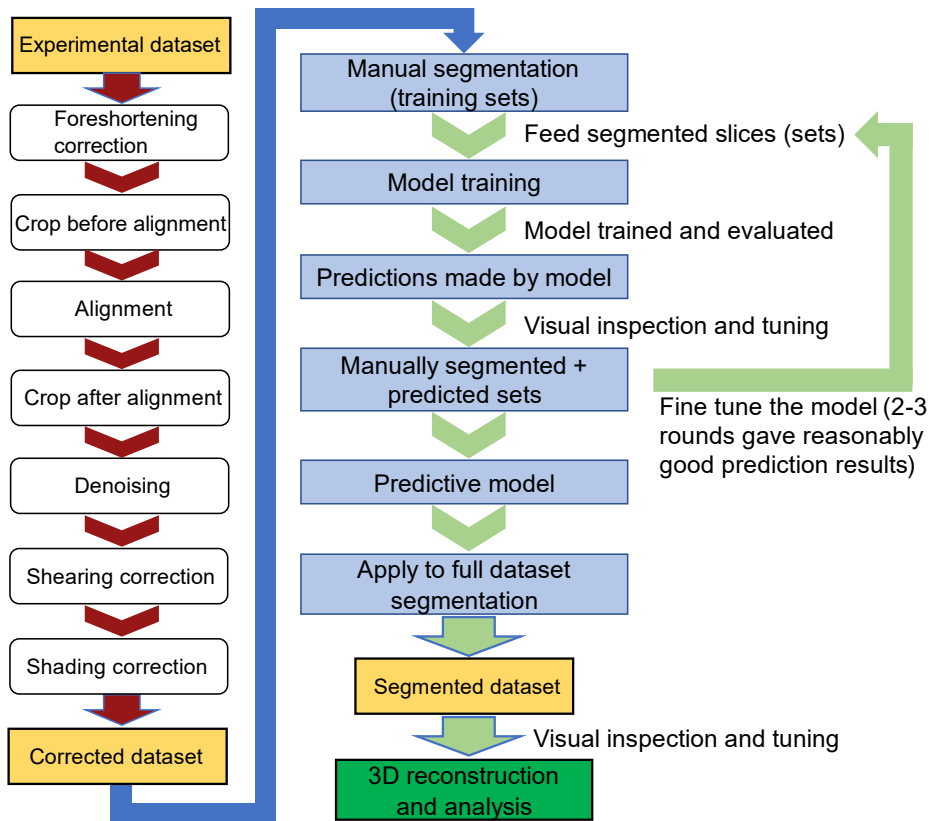
Fig 2. Workflow of FIB-SEM tomography dataset processing and deep-learning based segmentation procedure. Raw tomographic dataset obtained from experiment is first processed and corrected to obtained corrected dataset. This is also well-documented in these references[44,50-52]. Corrected dataset is then directly taken to initiate predictive model training starting with manual segmentation for training set (frames) preparation. Several built-in convolutional neural network models are preliminarily trained for comparison purposes and evaluated by both human visual inspection of predictions and scores achieved. The model with best predictions and highest score is further trained with more segmented sets (frames) and this process can iterate for a few times until it gives reasonably good predictions. Model training details can be found in Method section and key parameters listed in Table 2. The whole dataset is then segmented by this trained predictive model and hence a segmented dataset is obtained. Necessary visual inspection and fine tuning of this segmented result is carried out before eventually being analysed and 3D reconstructed. FIB-SEM tomography datasets are processed by using Avizo Standard 9.7.0 and deep learning segmentation performed in ORS Dragonfly.

230 *Table 2. Summary of key setup and parameters used for deep learning model training and segmentation.*

	2D U-Net	3D U-Net	Sensor 3D	2D FC-DenseNet56
Model details	Depth-level 4, initial filter count 64,	Depth-level 4, initial filter count 64, Number of input slices: 3	Number of input slices: 3	NA
Algorithm	Adadelta	Adadelta	Adadelta	Adadelta
Patch size	256	256	256	256
Stride ratio	0.2	0.2	0.2	0.2
Epochs number	100	100	100	100
Data augmentation	10	10	10	10
Loss function	ORSDiceLoss			
Frames trained in first round	10	10	10	10
Total frames trained	~20-25	NA	NA	NA
Workstation hardware	GPU: NVIDIA Quadro P5000; CPU: Intel(R) Xeon(R) Gold 6130 @ 2.10GHz with 64 processors; 384GB installed RAM; 30TB SSD storage.			
Total training hours	~6-8 hours	NA	NA	NA

3. Results

3.1 Scanning electron microscopy images

235   Example secondary electron SEM images of NT02 POCO graphite freshly fractured surface is given in Fig 3 (a-b). Fractured surface is uneven and shows finely grained surface texture with porosity also being exposed to viewing. The magnified SEM view in Fig 3 (b) shows the randomly but uniformly distributed porosity in NT02 POCO graphite with some example pores labelled by yellow arrows. Also shown in Fig 3 (c-e) are the example SEM cross-sectional
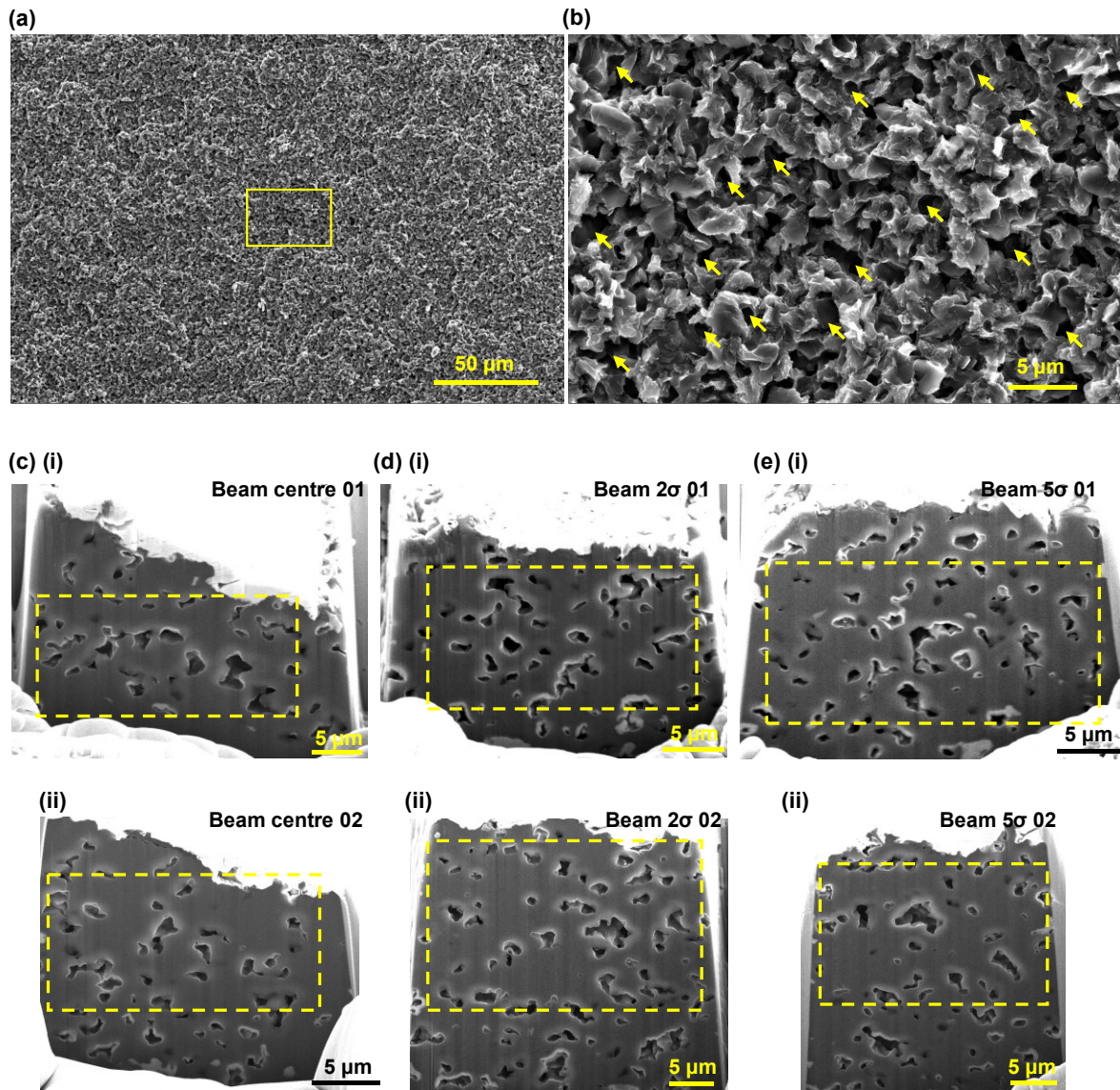240   views of milled NT02 POCO graphite.

Fig 3. Secondary electron SEM images of proton irradiated NT02 POCO graphite showing their texture and porosity. Shearing correction is not applied in these images. (a) SEM view of fractured surface of NT02 POCO taken at ~ beam 2σ radius location showing finely grained texture with porosity can hardly be resolved at this magnification and, (b) is the magnified view of the central region marked by the yellow box in (a). NT02 POCO has uniformly distributed and interconnected porosity across the entire region, as some example pores marked by yellow arrows in (b). (c-e) Raw FIB-SEM tomography images showing example cross-sectional views of milled volume at beam centre (c), 2σ (d) and 5σ (e) locations prior to data processing and artefact correction. The yellow dashed boxes indicate approximately the cropped, corrected and reconstructed 3D volumes as in Fig 5.

These six images remark the porosity examined at three locations across proton beam profile with two sites for each location. It is clear that NT02 POCO graphite's micrometre scale pores are still uniformly distributed in these volumes and are consistent with previous findings in

un-irradiated POCO ZXF-5Q graphite that there is predominantly fine porosity in this graphite grade with uniform spatial distribution[44]. Since the scale bars in these six images are 5 µm it is evident that NT02 POCO graphite has a considerable amount of fine porosities less than 1-2 µm in 2D dimensions. Segmented porosity per image slice (2D areal porosity) is plotted against slice number and this is shown in Fig 4. It can be seen that there is an overall lowered 2D porosity in the two datasets at beam centre of about 8%, compared to those from beam 2σ and 5σ locations of about 12 %. To explicitly investigate whether and how exactly these micrometre scale porosities have been modified by energetic proton irradiation, detailed analysis of these porosity structures was carried out by using ORS Dragonfly[45] deep learning-based segmentation, and subsequently 3D reconstruction and statistics performed in the same software, see Methods section. Results are given in Fig 5.
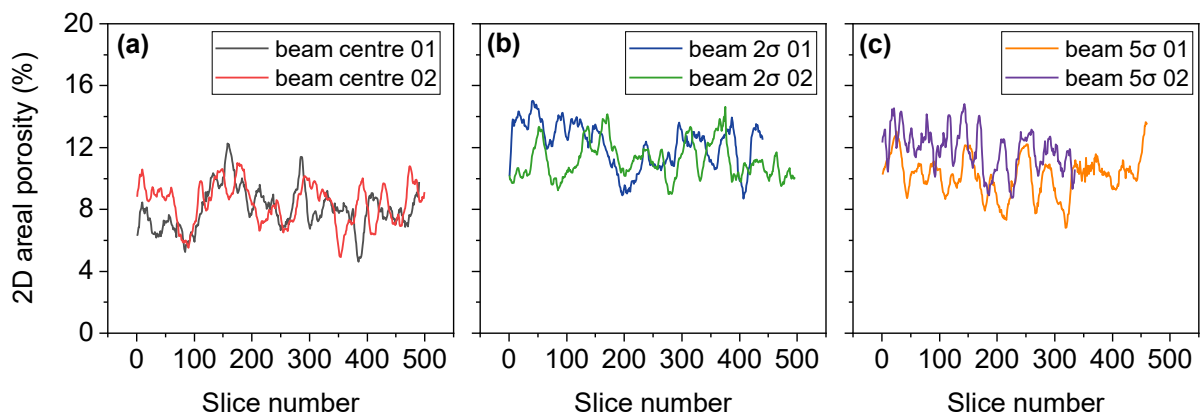

Figure 4. Porosity distribution across each image slice in FIB-SEM tomography datasets from (a) beam centre, (b) beam 2σ and, (c) beam 5σ radius locations. There is an overall lowered 2D porosity in the two datasets at beam centre compared to those from beam 2σ and 5σ locations.

3.2 Visualisation and 3D analysis of porosity

3D reconstructed porosity structure of the six FIB-SEM tomography datasets conducted on proton irradiated NT02 POCO are shown in Fig 5 with two datasets from each location, i.e., (a i-ii) at beam centre, (b i-ii) at beam 2σ radius and (c i-ii) at beam 5σ radius distance away from beam centre. Different colours are for labelling each individual pore and therefore, it can be seen there are a number of extremely large pores in all of these 6 volumes which are marked by a single colour. It is also clear that there is a large number of pores with relatively small sizes and distributed evenly across the volumes examined. These morphological features and

spatial distribution of NT02 POCO graphite are similar to the previous findings from un-irradiated POCO graphite which illustrates the high confidence in the current results.

The total volumetric percentage of porosity are determined. It is 8.02 vol.% and 8.40 vol.% at proton beam centre; 12.15 vol.% and 11.18 vol.% at beam 2σ radius; and 10.17 vol.% and 11.88 vol.% at beam 5σ radius, Fig 5. Porosity percentage is subject to ± 1 vol.% error maximum. Porosity percentage at beam centre appears to be the lowest. Further detailed analysis will be conducted. The last two images in Fig 5 (d i-ii) show the previous FIB-SEM data from un-irradiated pristine POCO graphite but segmented and analysed using the ORS Dragonfly software by following the same procedure as described in Methods section to be consistent. It can be seen that the equivalent diameter distribution is consistent with the previous data analysed by Avizo Standard software and the total porosity difference is only 1.5%, comparable to the reported porosity error[44]. Segmented image stacks are demonstrated by one supplementary animation video provided.

This decrease in the total porosity volumetric percentage from about 12 vol.% at 2σ and onwards down to about 8 vol.% at beam centre could be seen in Fig 5 (a-c). This decline can be further compared to the total porosity percentage from pristine POCO of 11.7 vol.% computed from ORS Dragonfly within a reconstructed volume of 4637 μm^3 as in Fig 5 (d), or compared to the previously reported 13.18 vol.% within a volume of 2962 μm^3 from the same dataset by Avizo Standard[44]. Since an average error of 1% in the porosity analysed in Avizo has been reported, the good consistency among either tomography data sets from NT02 POCO 2σ and 5σ radii, or between pristine POCO analysed by the two different software, implies that pristine POCO graphite sub-micrometre scale porosity should be around 12 vol.% and uniformly distributed through space. This decrease in porosity volumetric percentage at proton beam centre is discussed in more detail in Discussion section.

Further statistics of the pores are shown in Fig 6 based on the tomography data at beam 2σ radius as an example. Segmented 3D image stack of pores, Fig 6 (a), were classified by a variety of quantities such as volumes, surface areas and mean Feret diameters and so on by ORS Dragonfly's connected component analysis module with 3D visualisations made by its measurement inspector module. Examples shown in Fig 6 (c-f) are illustrating the spatial distribution of porosity categorised by their 3D volumes, i.e. < 1 μm^3, 1 − 2 μm^3, 2 − 5 μm^3 and

greater than 5 μm³ and coloured accordingly. It is apparent that very fine pores with volumes

310   less than 1 μm³ are uniformly dispersed within the entire space but only accounting for 7.5

vol.% of the porosity volume. It is believed that pores having volumes less than 5 μm³, as in

Fig 6 (c-e), are essentially isolated closed pores without strong connectivity. However, pores

having volumes greater than 5 μm³ are occupying 70.0 vol.% of porosity volume and they are

formed by interconnected open pores, as in Fig 6 (f). Fig 6 (b) shows the histogram of

315   calculated equivalent diameters within this rectangular volume. The vast majority of pores

have diameters less than 1 μm (56.2 % + 15.8 %= 72%) as in the insert pie chart. Only less than

7% of the pores have equivalent diameters larger than 2 μm. These findings agree with the

distribution statistics in previous work on un-irradiated POCO graphite[44].
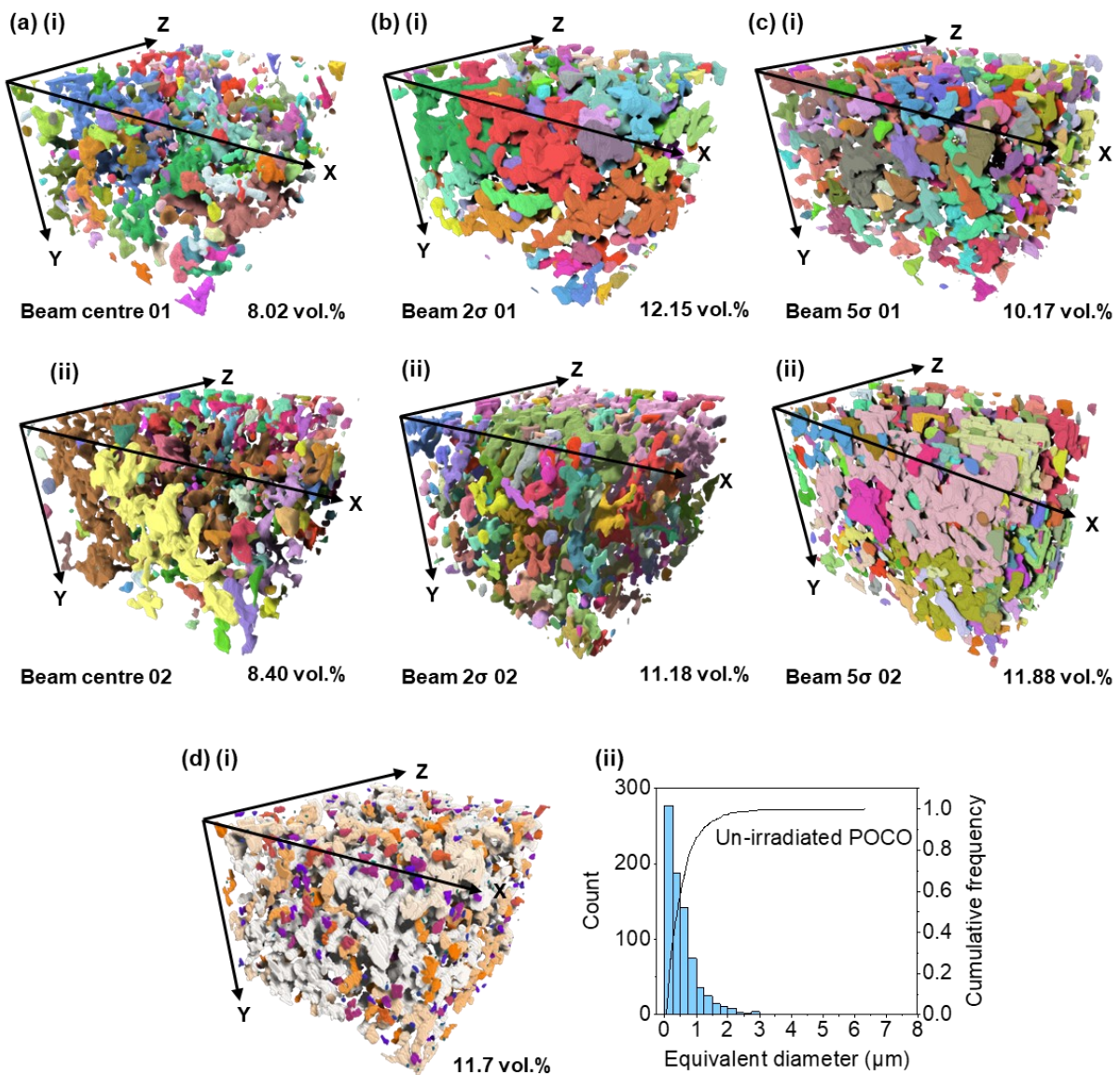
320 *Fig 5. 3D reconstruction of NT02 POCO graphite porosity structure revealed by FIB-SEM tomography across proton beam irradiation profile. (a i-ii) Porosity at proton beam centre showing volumetric percentage of 8.02 and 8.40 vol.%. (b i-ii) At 2σ beam radius with 12.15 and 11.18 vol.% porosity and, (c i-ii) At 5σ beam radius with 10.17 and 11.88 vol.% porosity. A number of large pores are formed by interconnected small pores. (d i-ii) Reconstructed porosity 3D structure from pristine POCO ZXF-5Q graphite without irradiation showing a*
325 *volumetric percentage of 11.7 vol.%, consistent with the numbers from (b-c) and previous work[44]. Reconstructed physical volume is 17.5 × 13.4 × 19.8 = 4637 μm³. The majority of pores has equivalent diameter of less than 1 μm in un-irradiated POCO graphite and other details have been published somewhere else[44]. Different colours are used for labelling each individual pore. The physical sizes of these reconstructed cuboid volumes are listed in the Table 1. All segmentation was done by deep-learning technique as described in the Methods section with 3D*
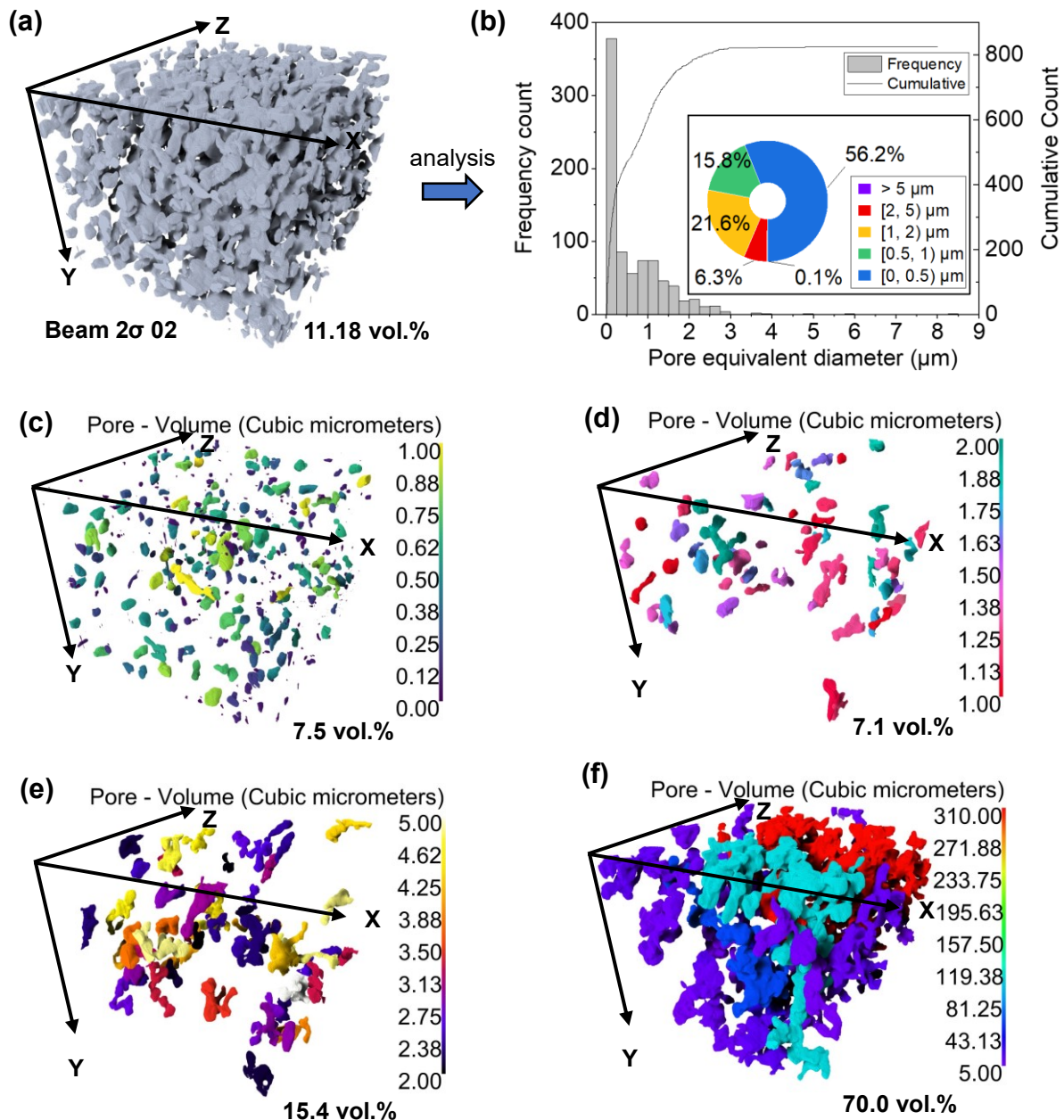330 *reconstruction and analysis also done in ORS Dragonfly software.*

Fig 6. An example showing porosity analysis of one of the FIB-SEM tomography data taken at beam 2σ distance towards beam centre. (a) Total porosity is 11.18 vol.% within this volume and this is taken to further detailed analysis including classifying pore sizes into several ranges and labelling and computing the volumetric percentage. (b) Computed pore volumes are converted into equivalent diameters by taking their analogues as sphere and therefore, histogram of these diameters can be plotted. It is evident that 72 % (56.2 %+15.8 %) of the pores in this space has equivalent diameters less than 1 μm. However, only 0.1% of the pores have equivalent diameter greater than 5 μm that are formed by interconnection. (c-f) Pores having volume of less than 1 μm³ are uniformly distributed, accounting for 7.5 % of the pore space. The vast majority of porosity space (70.0 vol.%) is occupied by pores having volumes greater than 5 μm³ as in (f).
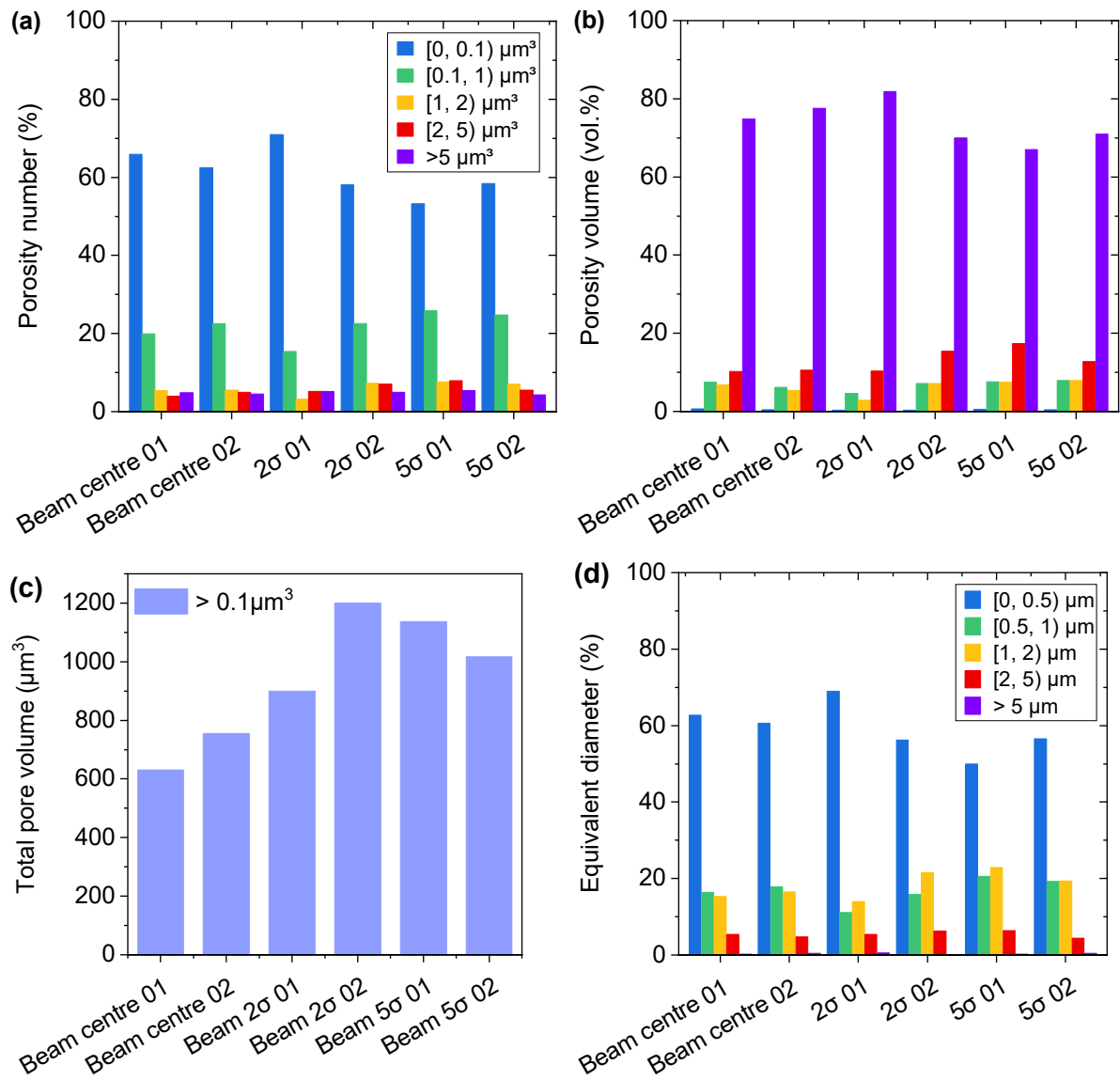
3.3 Porosity statistics

Detailed statistics of NT02 POCO porosity are given in Fig 7. Porosity volume is classified into five groups, with the smallest range being less than 0.1 μm^3 and the largest being greater than 5 μm^3, as shown in Fig 7 (a-b). Data from all six tomography datasets are plotted for side-by-side comparison, including two datasets from each of the three milling locations. In Fig 7 (a), approximately 55 - 70% of the pores have a volume less than 0.1 μm^3, 15 - 25% of the pores have a volume between 0.1 - 1 μm^3, whereas only about 4.2 - 5.3% of the porosity is larger than 5 μm^3 in all six tomography datasets. The volumetric percentage values of this porosity in the rectangular volume reconstructed are plotted in Fig 7 (b) and categorized by their sizes. It is evident that although the number of pores with sizes smaller than 0.1 μm^3 accounts for about 55 - 70% of the population, they only occupy about 0.5 vol.% of the porosity space. It is those pores larger than 5 μm^3, formed by interconnected small pores, that fill over 60 - 85 vol.% of pore volumes, but only account for about 5% of the population.

The main message here is twofold: 1) Pores in NT02 POCO graphite are dominated by largely interconnected ones but there are very few of them, meaning a few large pores constitute the majority of the overall porosity. The vast majority of porosity population (85%) consists of isolated closed pores with sizes smaller than 1 μm^3 but this fraction of pores only occupies about 10 vol.% of the pore volume. 2）These findings agree well with the distribution statistics previously found in the FIB-SEM tomography of un-irradiated pristine POCO ZXF-5Q graphite. Since pores smaller than 0.1 μm^3 contribute insignificantly (0.5 vol.%) towards total measured porosity. Pores that are larger than 0.1 μm^3 have been summed up to give total pore volume and plotted in Fig. 7 c. The decrease in total pore volume is apparent for the two datasets at beam centre area in Fig. 7 c. Converting all 3D pore volumes into equivalent diameters gives the plot in Fig 7 (d). It shows that pores having diameter less than 0.5 μm accounts for 50 – 70 % of porosity population which is consistent with Fig 7 (a). Only less than 0.5 % of the pores having equivalent diameter greater than 5 μm.

370

Fig 7. Statistics of NT02 POCO porosity from the 6 FIB-SEM tomographies. Porosity has been analysed by their 3D volumes as well as 3D equivalent diameters calculated by taking their digital analogues of spheres, with percentages computed subsequently. These columns are plotted for side-by-side comparison of porosity variation against locations along proton beam profile. Each of the locations has two tomographies giving greater statistical

375 *confidence. (a) Porosity number fraction categorised by their 3D volumes. Pore volumes less than 0.1 μm^3 are labelled by blue colour and greater than 5 μm^3 by purple colour, and so on. About 55- 70 % of pores have volume less than 0.1 μm^3 in all 6 tomographies. (b) Porosity volume fraction also classified by their 3D sizes and colour scheme is the same as in (a). Pores having volumes greater than 5 μm^3 accounts for 60-80 vol.% of the porosity structure, relatively consistent across these tomographies. (c) Total pore volume by summing up all the pores*

380 *larger than 0.1 μm^3. A reduction of total pore volume at proton beam centre is clear. (d) Columns of fractional equivalent diameter with diameter less than 0.5 μm being coloured in blue and it is about 55 − 70 % of the porosity in all six datasets.*

3.4 Impact of sampled volume on porosity

The decrease in total pore volume percentage at beam centre is further explicitly examined by plotting pore population against reconstruction volume as in Fig 8 (a), to verify whether the difference is caused by different physical volumes reconstructed. The key points that can be inferred from Fig 8 (a) include the following:

(1) Although reconstructed physical volumes of six tomography datasets are different, the number of pores is proportional to the volume sizes, i.e., larger reconstructed volume revealed more pores, and this is seen by comparing the first three datasets to the last three in Fig 8 (a).

(2) By comparing the two datasets at beam 2σ in Fig 8 (a) and Fig 5 (b), it is evident that the change in physical volumes reconstructed does not affect the total porosity volumetric percentage since their porosity difference is only ~ 1% as in Fig 5 (b).

(3) By comparing beam centre datasets and 2σ 01 in Fig 8 (a), their pore numbers are similar but the porosity volumetric percentages differ by ~ 4 vol.%, which is 12.15 vo.% at 2σ 01 as opposed to 8.0 vol.% and 8.40 vol.% at beam centre.

These indicate that the size of sampling volume did not affect total porosity volumetric percentage, and the change of total porosity is not a biased result from either reconstructed physical volume or segmentation techniques used (informed by Fig 5 (d) and ref[44]).

The volumetric fraction of all pores larger than 0.1 μm^3 in relation to the total volume reconstructed is plotted in Fig 8 (b), categorised by their sizes. It is clear that there is a noticeable size decrease in the pores with volumes > 0.1 μm^3 in the two datasets from beam centre, i.e., ~ 8 vol.% as compared to over 10 vol.% from the others from beam 2σ and onwards. The most noticeable change is in the size range of $0.1 - 5$ μm^3. Aspect ratio for porosity having volume greater than > 0.1 μm^3 is plotted in Fig 8 (c). Aspect ratio is computed by ORS Dragonfly using the ratio between the minimum and maximum rigid body inertia eigenvalues. An aspect ratio of 1, 0.5 and 0 represents a perfect 3D cube/sphere, 2D square/circle and a 1D rod-like object with 1 voxel wide, respectively. It can be seen from Fig 8 (c) that aspect ratios are independent of locations with no definitive trend of change. This implies that porosity volumes at beam centre are uniformly reduced in all directions with no geometric preference.
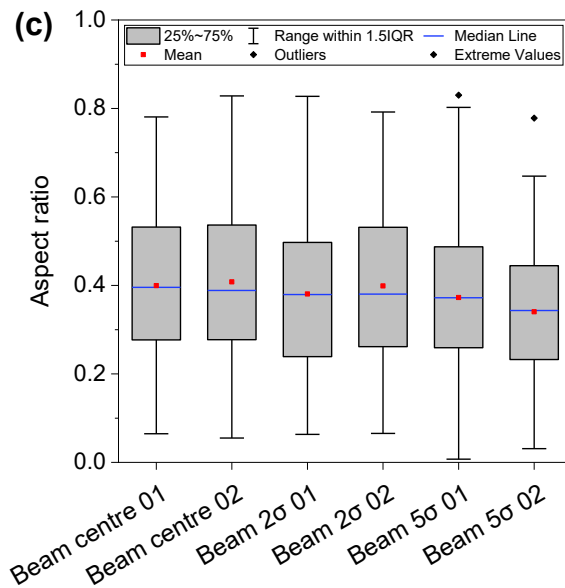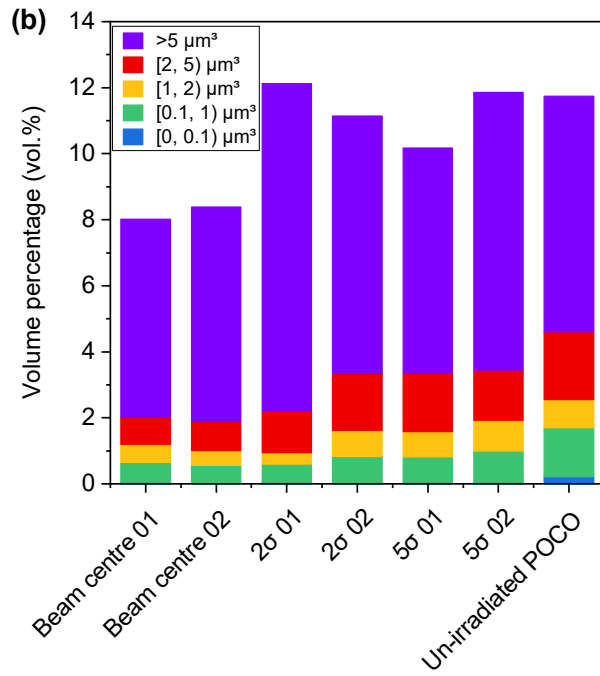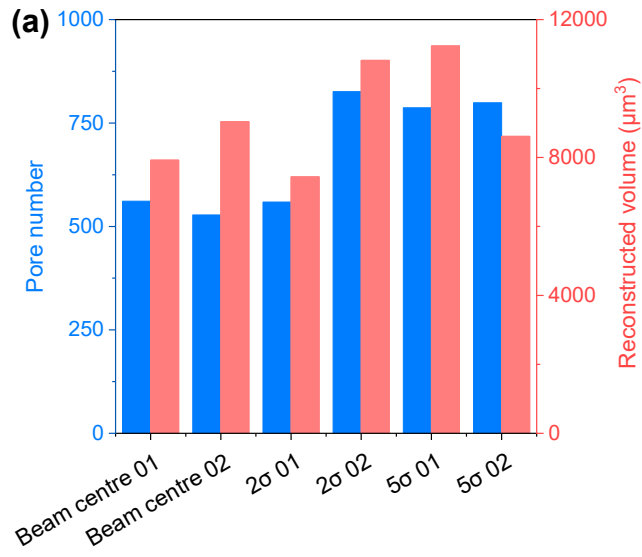
415 *Fig 8. (a) Number of pores plotted against physical volumes reconstructed for side-by-side comparison in these FIB sites, verifying that reduced porosity volumetric percentage at beam centre is not due to sampling volume difference, as can be seen by comparing 2σ 01 and 2σ 02 and the number from Fig 5b. (b) A reduced volumetric percentage of pores having sizes > 0.1 μm³ have been identified and it is the drop of these relatively large pores in the two FIB sites at beam centre that caused total percentage drop as in Fig 5. (c) Measured porosity aspect ratios.*

420 *Aspect ratio of 1, 0.5 and 0 represents a perfect sphere, circle and 1D rod, respectively, see main text for descriptions.*

4. Discussion

This work concerns the porosity change of POCO ZXF-5Q graphite that has undergone high-
425 energy proton beam irradiation. The difference between pulsed proton beamline environment and graphite-moderated thermal fission reactors shall be firstly briefly described in terms of the following three aspects to better appreciate the problem:

(1) Effect of flux. The typical flux in a thermal or mixed spectrum fission reactor is about 10^{-7} dpa/s[58], and it is about 10^{-6} dpa/s for fast fission reactor and fusion reactor[58,59]. Whereas the
430 instantaneous flux in high energy proton beam could reach $5\text{-}6 \times 10^{-3}$ dpa/s[58]. Extensive research has been conducted to examine the impact of flux on dimensional and material properties in graphite[60,61]. Material test reactors (MTRs) with higher fluxes have been used to accelerate data acquisition compared to power-producing reactors[62-64]. Initially, it was hypothesised that varying fluxes, despite identical fluence and neutron energy spectra, lead
435 to distinct property changes due to effectively different net damage rate that is also a function of irradiation temperature and time inside reactor environment. In this context, the concept of equivalent temperature[65] was proposed to account for such net damage rate effect in graphite, supported by experimental data at 350 °C and below by Eason *et al*[66], with little or no clear evidence to support its use in the temperature range of 350–650 °C [66]. Considering the peak
440 irradiation temperature in NT02 POCO is below or very near to the temperature boundary quoted by Eason *et al*[66]. and the measured results will be primarily compared with graphite materials irradiated under different fluxes, the effect of flux is likely to play a role in the observed dimensional and porosity change, and to be specifically studied via controlled irradiation experiment.

445   (2) Pulsed and continuous irradiation. To the best of the authors' knowledge, to date, there have been no openly published studies on the disparities in irradiation effects between pulsed and continuous proton irradiation in nuclear graphite. However, modelling work on metals indicated that the impact of proton irradiation, for instance, at a specific dose or dpa level, might be influenced by whether protons were delivered in a cyclic pulsed or continuous

450   manner at a pulsing frequency of 1 Hz[67]. Simulation of 800 MeV pulsed proton irradiation from Kmetyk et al.[68] suggested that pulsing the irradiation would only affect metal material swelling indirectly and new effects would only be produced if the pulse times were greater than or comparable to vacancy and interstitial reaction times, partially due to radiation induced thermal pulses. Exact differences between pulsed and continuous proton irradiation

455   on graphite structural change will need to be studied through well-controlled experiment in future.

       (3) Irradiation damage caused by protons and neutrons. A significant amount of property and structural change data of nuclear graphite, as well as the understanding of these changes, originated from historic graphite-moderated thermal fission reactors data[69-72] and MTR

460   irradiation experiments[62,63,73]. Although current understanding of the similarities and differences in structural and property changes in nuclear graphite under proton and neutron irradiation is not yet fully established, there do exist sparse published work on proton irradiation behaviour of nuclear graphite to emulate that from neutron[74-77]. Hove[78] showed that there is very little difference from graphite property changes induced by neutron and

465   proton irradiation (8.8 MeV) but that set of experiments were conducted at much lower temperature (103-523 K) as well as proton energy than NuMI experiment reported in this work. Was et al.[79-81], although mainly focused on metal materials, suggested that it is appropriate to emulate neutron irradiation effects by protons since the observed microstructural and property changes were in good agreement with reactor irradiation. Attempts to directly study

470   high energy proton beam irradiation (160 MeV) on fine-grained graphite have been made by Simos et al. in searching for suitable candidate target graphite materials for proton beamline[2,31,32,82]. Proton irradiation induced bulk and crystal dimensional change and property changes including Young's modulus, tensile strength, coefficient of thermal expansion (CTE) in these fine-grained target graphites were compared with the data from historic grades

475   irradiated by neutrons, suggesting good agreement in their work[31,82].

Given the limited availability of experimental data, understanding of the structural and property changes induced by proton irradiation in nuclear graphite, especially POCO graphite at relatively low doses and relevant beamline irradiation temperatures, is constrained. Recourse has to be made to the property changes observed in other grades of graphite with most of which were irradiated by neutrons, as discussed in the following paragraphs.

Porosity change with irradiation and temperature is an important part of graphite structural evolution. It is generally accepted that Mrozowski type microcracks can be directly modified by irradiation and it predominantly determines nuclear graphite crystal and bulk dimensional change with the latter shows the classical 'shrink then swell' behaviour. At the early low dose stage of irradiation before 'turn-around', closure of Mrozowski cracks is mainly caused by graphite crystallographic c-axis expansion due to interstitial clusters and subsequent new basal planes created[83], thermal expansion[20], and deformation and buckling of basal planes[84-87]. Together with a-axis contraction caused by coalescence of vacancies within basal planes[83], effect of Poisson's ratio[88] and concomitant effect from basal plane buckle and ruck and tuck[85], a net bulk volumetric shrinkage is usually seen at this stage. Crystal dimensional change in both highly annealed pyrolytic graphite (HAPG)[88] and PGA graphite[89] showed continuous growing and shrinkage in c-axis and a-axis respectively, with a much faster dimensional change rate observed at irradiation temperatures lower than 250 °C. Rapid expansion in the c-axis could have rapidly consumed the available Mrozowski cracks leading to earlier 'turn-around' in NT02 POCO graphite at low irradiation temperatures. Heggie *et al.*[85] proposed that another dominant mechanism responsible for graphite crystal c-axis expansion below irradiation temperature of 250 °C, apart from Frenkel pairs and new basal plane formation by interstitial clusters, is permanent basal plane nano-buckling, and it is ruck and tuck when above 250 °C. However, as also mentioned in the recent work by Jiang *et al.*[90], due to the local temperature gradient caused by proton energy deposition and cooling channels and thermal cycles caused by the pulsed beams, it has not been possible to trace the exact local distribution and history of irradiation temperature in the POCO graphite target fin studied in this work. Hence, it still remains unclear whether the observed crystal dimensional change at proton beam centre area is faster than at the edges. Whether NT02 POCO graphite crystal dimensional change at proton beam centre area is accompanied by the mechanisms proposed

by Heggie et al.[85] requires further investigation. Future high-resolution TEM analysis needs to be carried out to specifically investigate crystal deformation and c-axis expansion mechanisms in NT02 target POCO graphite.

510   Closure of Mrozowski cracks has been found in HOPG and/or nuclear graphite in such experiment from the work by Wen et al.[22] (dose/fluence not reported), Karthik et al.[91], Shen et al.[92] and Johns et al.[93]. In the recent work by Karthik et al. on neutron irradiated IG-110 and NBG-18 graphite[94], there was no significant change in Mrozowski cracks that has been found in both filler particle and binder matrix at initial low dose stage of < 2 dpa at ~ 450 and ~ 670 °C.

515   Only when irradiated to ~ 6.7 dpa could closure of Mrozowski cracks in a length scale of hundreds of nanometres be clearly seen. For NT02 POCO graphite, although no lenticular thermal shrinkage crack at micrometre scale such as calcination cracks have been found, there do exist Mrozowski type cracks at nanometre scale[46,95]. Post irradiation examination (PIE) of POCO fins extracted from the same MINOS/MINERvA irradiation experiment using ex-situ

520   TEM analysis suggested no quantifiable modification of Mrozowski cracks under NuMI beamline irradiation condition[95]. But it was also argued by these authors that this could be the fact that only small volumes were examined and local variation could not be ruled out[95].

Hall et al.[29] and Haag et al.[30] demonstrated large lenticular cracks (at hundred micrometre scale) played a role in accommodating expansion of c-axis which subsequently affected the bulk

525   dimensional change and 'turn-around' behaviour in Gilsocarbon graphite, and hence these large cracks were termed as 'accommodation porosity'. It is then necessary to investigate whether the micrometre scale porosity in POCO graphite has been modified by proton irradiation which is the key incentive of present work. The most direct evidence from this work is the apparent decrease in these micrometre scale porosity (pores with sizes > 0.1 μm^3)

530   volume at beam centre area as shown in Fig 5 and 8, suggesting that not only can nano-size Mrozowski type lenticular cracks accommodate c-axis expansion, but also this type of large micrometre size porosity can accommodate local volume expansion. In this case of POCO ZXF-5Q graphite where filler particles are milled to microfine-grained sizes, no large lenticular cracks of the same type studied by Hall et al.[29] and Haag et al.[30] were observed (see

535   Materials section). The globular and interconnected pores distributed within and in between filler grains will instead serve as accommodating porosity in addition to nano-scale Mrozowski cracks. However, other mechanisms that could have potentially contributed

towards the observed dimensional change such as irradiation creep and gas production damage cannot be ruled out at this stage.

540 Usually, nuclear graphite volume shrinkage rate will decrease when it is irradiated to higher doses where bulk volume reaches a minimal. This is then followed by volumetric swelling as a result of the formation of new defects and pores. One recent experimental work by Contescu et al.[96] on a superfine-grained G347A graphite neutron irradiated to cover the full dimensional change process showed drastic increase in sub-micrometre scale porosity with volumes < 0.1

545 um[3] at very high doses after 'turn-around', accompanied by the multiplication and growth of mesopores (tens of nanometres). The 'turn-around' point for G347A graphite at 300 °C[63] is ~ 18 dpa. This value is ~ 18 dpa for the medium-grained near-isotropic Gilsocarbon graphite at 430 °C[28], and it is ~ 18 dpa, ~15 dpa and ~12 dpa for fine-grained IG-110 at 300 °C[97], 600 °C[98] and 750 °C[99] respectively. The higher the irradiation temperature, the more rapid dimensional

550 change and earlier the 'turn-around' point[24,28]. Considering that a peak irradiation temperature of ~350-370 °C was estimated at the proton beam centre on NT02 POCO with a reported displacement damage of ~1 dpa[31], it is highly unlikely that material at the beam centre had passed its 'turn-around' point. However, instead of bulk shrinkage, it exhibited bulk dimensional swelling of ~ 3.8 – 4.3 %[31,95] at such low dose. In fact, direct bulk dimensional

555 swelling at low doses has not only been reported in NT02 POCO graphite but also in other various grades of medium-/fine-grained graphite irradiated at different temperatures including ETP-10, IG-110U, NBG-10, Gilsocarbon graphite and some historic POCO grades[33-36,83], which has been postulated to be caused by irradiation-induced residual stress relaxation at low doses[34,100]. But it was argued by Marsden et al. that there is currently no evidence for

560 this hypothesis[28,101]. Further to these, the POCO ZXF-5Q graphite has been graphitised at 2500 °C, lower than the 'standard' ~2800 °C for conventional nuclear graphite grades. Although it has been shown that reducing graphitisation temperature would increase dimensional change rate[24], there is no direct evidence showing lower graphitisation temperature would reverse the dimensional change from shrinkage to swelling at low dose

565 stage.

The flux, fluence and temperature distributions in graphite target fin led to different rates of dimensional change within the target fin component. These stresses would in turn alter the dimensional changes through the mechanism of irradiation creep. The ratio between the bulk

dimensional swelling at target fin beam centre and target fin edge has been reported to be

570   about 1 to 2, meaning a gradient of stress was generated[95]. Modelling of proton irradiation induced swelling in NT02 POCO fins by Bidhar *et al*.[47] suggested a compressive stress of 150 MPa at beam centre due to constraint from surrounding materials, which is an upper bound due to the lack of such POCO graphite creep strain data. As such, the reduction in porosity volume could have been affected by irradiation creep process. Practically, creep strain is

575   regarded as the difference between dimensional changes under loaded and unloaded conditions. Upon irradiation, if the unloaded graphite expands (as observed in the current POCO graphite), applying a compressive load diminishes the expansion, while a tensile load amplifies it. The only publicly available dimensional change data of POCO graphite at a lowest irradiation temperature of ~ 400°C are those from POCO AXF-8Q1 and AXZ-5Q1 from

580   Pitner[36], AXF-Q1 from Kelly[35] and AXF-5Q to a very low dose (0.08% dimensional change at 1×10^{20} n/cm^2) at 380 - 450ºC from Platonov *et al*[102]., all showing negligible dimensional changes when neutron irradiated to a few dpa without irradiation creep. This means that it is not clear how much irradiation creep has contributed towards the observed bulk dimensional swelling of ~ 4.3 % of NT02 POCO fin at proton beam centre area. Campbell *et al*.[46,103] studied proton

585   irradiation creep mechanisms in POCO graphite in which the lowest temperature achieved was 700 °C. The highest creep strain at this temperature was about 0.5% under 20 MPa tensile stress, creep rate of 8.24×10^{-3} %/hr and a dose rate of 5.52×10^{-7} dpa/s to a final dose of ~0.11 dpa after 55 hours of irradiation. They found that high temperature creep mechanism in POCO graphite comply with stress-induced preferential absorption (SIPA) of defects at

590   dislocations, suggesting vacancy lines and loops disassociate into dislocations, challenging the traditional theory of interstitial loop formation and growth. This may provide insights for the creep and dimensional change behaviour in target graphites in future LBNF-DUNE and T2K experiment as the irradiation temperature will be pushed beyond 700 °C[42,58].

With respect to the effect of irradiation creep on micrometre scale porosity change, there are

595   very limited data in literature correlating irradiation creep to micrometre scale porosity in nuclear graphite. Snead *et al*. reported a gradual decrease in the average size of nanoscale porosity (2 - 50 nm) with increasing irradiation dose in IG-110 graphite when it is compressively stressed. Nitrogen adsorption revealed that total pore volume decreased and then increased with the minimal porosity volume occurring at 3.36 dpa at ~ 400 °C. However,

600   they argued that porosity evolution at this length scale contributed insignificantly to the overall dimensional change of IG-110 graphite[104]. Oku *et al.* reported partial disappearance of pores having diameter less than 10 μm, by using mercury porosimetry, of a medium-grained near-isotropic SM1-24 graphite that has undergone irradiation creep test under tensile stress up to ~ 1.1 dpa at ~ 900 °C, with the total porosity decreased by 4.6 %. But it was argued that

605   the contribution of porosity closure towards irradiation creep strain is uncertain[105]. Therefore, the exact correlation between irradiation creep and (sub-) micrometre scale porosity under applied stresses is yet to be established as they appear to vary with the type of graphite and temperature. This is an area requires a significant amount of future work on graphites that have experienced well-controlled irradiation creep experiment such as UK's ACCENT

610   programme and Germany's ATR-2 graphite irradiation creep test at DISCREET facility[106-109]. As operational temperatures become higher, thermal stress gradients become more pronounced, and beamline irradiation experiments become more prolonged, irradiation creep is also likely to become more profound in future leading to the desired understating of irradiation induced structural changes in fine-grained graphite.

615   Lastly, another complication in the damage of NT02 target graphite is the production of helium/hydrogen gas via interaction with high-energy proton beam, potentially causing additional microstructural change and property degradation. There are published research reporting graphite structural changes caused by gaseous products but mostly from pyrolytic graphite. Twinned surface with blisters containing helium (He) and deuterium (D) gas that

620   can grow laterally by cleaving into graphite layers was reported by Bacon *et al.*[110]. Chernikov *et al.*[111] implanted pyrolytic graphite with $^4He^+$ of 40 keV and 3.5 MeV at temperatures of 300 K and 770 K, showing irradiation induced swelling, creation of pressurised helium bubbles and the exfoliation of the layers. Surface erosion was observed in high density pyrolytic graphite implanted by 100 keV $^4He^+$ (accompanied with cone structure containing helium gas)

625   and 200 keV H_2^+ (accompanied with circular blisters) by Sone *et al*[112]. Lenticular opening, twin networks and spherical bubbles were reported from HOPG implanted by He^+ and D^+ at various temperatures by Niwase *et al.*[113]. Kelly *et al.*[114] reported ^{10}B-doped HOPG at 650°C led to increased dimensional change and layer delamination partly due to helium transmuted from ^{10}B that are trapped in cavities, but the effect from He and ^{10}B could not be separated due

630   to radiation damage clustering by ^{10}B. Helium production rate in Fermilab's MINOS

experiment has been estimated to be ~2200 appm and this number is estimated to be ~ 5500 appm and ~ 3600 peak appm in NOvA experiments running at 700 kW and 1 MW (AIP) beam power[115]. There seems to be a gap in literature in terms of nuclear graphite porosity evolution with gas production in both nuclear fission and accelerator target systems. It then remains unclear if POCO graphite's sub-micrometre scale porosity has been modified by He/H$_2$ gas production in NT02 target environment and further work is greatly desired.

5. Conclusions

Porosity characterisation of an ex-service POCO ZXF-5Q graphite material experienced high-energy high-intensity proton irradiation in the NT02 target system in Fermilab's NuMI beamline has been conducted. Sub-micrometre scale porosity has been imaged by six high resolution FIB-SEM tomography across proton beam fluence and temperature gradients in the fin. 3D FIB-SEM tomographic datasets are segmented by state-of-the-art deep learning-based segmentation techniques enabling subsequent 3D reconstruction and detailed statistics analysis. It has been found that there is a volume decrease in relatively large pores (volumetric reduction of pores having volumes > 0.1 μm^3) at proton beam centre location, corresponding to a reported irradiation dose and temperature of a few dpa and ~350 - 370 °C maximum in open literature.

Although the reduction of micrometre porosity volume at proton beam centre area of NT02 POCO graphite has been attributed to bulk dimensional swelling and a considerable amount of in-depth discussions have been presented, separating individual contributing factors, such as irradiation flux, temperature gradient and thermal cycles, irradiation creep, thermo-mechanical stresses and gas production damage, from observed dimensional and porosity change has not been possible. There is a huge knowledge gap between nuclear reactor graphite and pulsed proton accelerator graphite target material due to their different service conditions. Future work on characterising POCO graphite particularly on those experienced well-controlled irradiation experiment is greatly desired to help discern the effect from various factors towards the observed irradiation induced structural and property changes in target graphite materials.

Acknowledgement

Credit of Authorship

M. J.: Investigation, experiments, formal analysis and data curation, writing – original draft & editing. K. A.: Resources, writing - review & editing. G. L.: Resources, writing - review & editing. F. P.: Resources, writing - review & editing. D.L.: Conceptualization, resources, methodology, funding acquisition, supervision, writing - review & editing.

References

1   Nakadaira, T. The graphite target for J-PARC neutrino beam-line. *Journal of Radioanalytical and Nuclear Chemistry* **305**, 777-782, doi:10.1007/s10967-015-4120-7 (2015).

2   Simos, N. *et al.* Irradiation damage studies of high power accelerator materials. *Journal of Nuclear Materials* **377**, 41-51, doi:10.1016/j.jnucmat.2008.02.074 (2008).

3   Thomason, J. The ISIS spallation neutron and muon source—The first thirty-three years. *Nuclear Instruments and Methods in Physics Research Section A: Accelerators, Spectrometers, Detectors and Associated Equipment* **917**, 61-67 (2019).

4   Torregrosa Martin, C. L. *et al.* First prototypes of the new design of the CERN's antiproton production target. *Material Design & Processing Communications* **1**, e38 (2019).

5   Zhang, W.-t. *et al.* Microstructure and molten salt impregnation characteristics of a micro-fine grain graphite for use in molten salt reactors. *New Carbon Materials* **31**, 585-593, doi:10.1016/s1872-5805(16)60034-3 (2016).

6   Lee, J. J. *et al.* Protection of graphite from salt and gas permeation in molten salt reactors. *Journal of Nuclear Materials* **534**, 152119 (2020).

7   Song, J. *et al.* Preparation of binderless nanopore-isotropic graphite for inhibiting the liquid fluoride salt and Xe135 penetration for molten salt nuclear reactor. *Carbon* **79**, 36-45 (2014).

8   McCoy, H. *et al.* New developments in materials for molten-salt reactors. *Nuclear applications and technology* **8**, 156-169 (1970).

9   Marsden, B., Jones, A., Hall, G., Treifi, M. & Mummery, P. in *Structural Materials for Generation IV Nuclear Reactors*   495-532 (Elsevier, 2017).

10   Freeman, H. M. *et al.* On the nature of cracks and voids in nuclear graphite. *Carbon* **103**, 45-55, doi:10.1016/j.carbon.2016.03.011 (2016).

11   Karthik, C., Kane, J., Butt, D. P., Windes, W. E. & Ubic, R. Microstructural characterization of next generation nuclear graphites. *Microscopy and Microanalysis* **18**, 272-278 (2012).

12   Arregui-Mena, J. D. *et al.* Multiscale characterization and comparison of historical and modern nuclear graphite grades. *Materials Characterization*, 112047 (2022).

13   Liu, D. & Cherns, D. Nano-cracks in a synthetic graphite composite for nuclear applications. *Philosophical Magazine* **98**, 1272-1283, doi:10.1080/14786435.2018.1433886 (2018).

14   Baker, D. Graphite as a neutron moderator and reflector material. *Nuclear Engineering and design* **14**, 413-444 (1971).

15   Joyce, M. R., Marrow, T. J., Mummery, P. & Marsden, B. J. Observation of microstructure deformation and damage in nuclear graphite. *Engineering Fracture Mechanics* **75**, 3633-3645, doi:10.1016/j.engfracmech.2007.11.003 (2008).

16   Liu, D. *et al.* Towards understanding the influence of porosity on mechanical and fracture behaviour of quasi-brittle materials: experiments and modelling. *Int J Fract* **205**, 57-72, doi:10.1007/s10704-017-0181-7 (2017).

17   Hodgkins, A., Marrow, T. J., Wootton, M. R., Moskovic, R. & Flewitt, P. E. J. Fracture behaviour of radiolytically oxidised reactor core graphites: a view. *Materials Science and Technology* **26**, 899-907, doi:10.1179/026708309x12526555493477 (2013).

18   Liu, D. & Flewitt, P. E. Deformation and fracture of carbonaceous materials using in situ micro-mechanical testing. *Carbon* **114**, 261-274 (2017).

19   Liu, D., Heard, P. J., Nakhodchi, S. & Flewitt, P. E. J. in *Graphite Testing for Nuclear Applications: The Significance of Test Specimen Volume and Geometry and the Statistical Significance of Test Specimen Population*   Ch. Stp157820130127, 84-104 (2014).

20   Sutton, A. & Howard, V. The role of porosity in the accommodation of thermal expansion in graphite. *Journal of Nuclear Materials* **7**, 58-71 (1962).

21   Mrozowski, S. MECHANICAL STRENGTH, THERMAL EXPANSION AND STRUCTURE OF COKES AND CARBONS. (Buffalo Univ., 1954).

22   Wen, K., Marrow, J. & Marsden, B. Microcracks in nuclear graphite and highly oriented pyrolytic graphite (HOPG). *Journal of Nuclear Materials* **381**, 199-203, doi:10.1016/j.jnucmat.2008.07.012 (2008).

23   Hacker, P. J., Neighbour, G. B. & McEnaney, B. The coefficient of thermal expansion of nuclear graphite with increasing thermal oxidation. *Journal of Physics D: Applied Physics* **33**, 991 (2000).

24   Brocklehurst, J. & Kelly, B. Analysis of the dimensional changes and structural changes in polycrystalline graphite under fast neutron irradiation. *Carbon* **31**, 155-178 (1993).

25   Kelly, B. The elastic constants of polycrystalline carbons and graphites. *Philosophical Magazine* **9**, 721-737 (1964).

26   Kelly, B. & Foreman, A. The theory of irradiation creep in reactor graphite—The dislocation pinning-unpinning model. *Carbon* **12**, 151-158 (1974).

27   Marsden, B. J. & Hall, G. N. in *Comprehensive Nuclear Materials*   325-390 (2012).

28   Marsden, B. J. *et al.* Dimensional change, irradiation creep and thermal/mechanical property changes in nuclear graphite. *International Materials Reviews* **61**, 155-182, doi:10.1080/09506608.2015.1136460 (2016).

29   Hall, G., Marsden, B. J. & Fok, S. L. The microstructural modelling of nuclear grade graphite. *Journal of Nuclear Materials* **353**, 12-18, doi:10.1016/j.jnucmat.2006.02.082 (2006).

30   Haag, G. in *Engineering Challenges Associated with the Life of Graphite Reactor Cores.* (eds P. E. J. Flewitt & A. J. Wickham) - (The National College).

31   Simos, N. *et al.* 120 GeV neutrino physics graphite target damage assessment using electron microscopy and high-energy x-ray diffraction. *Physical Review Accelerators and Beams* **22**, doi:10.1103/PhysRevAccelBeams.22.041001 (2019).

32   Simos, N. *et al.* Low-temperature proton irradiation damage of isotropic nuclear grade IG-430 graphite. *Journal of Nuclear Materials* **542**, 152438 (2020).

33   Maruyama, T. & Li, Z. Dimensional changes and thermal conductivity by annealing and its relation to the defect concentration and stored energy release of neutron-irradiated graphite. *Journal of Nuclear Science and Technology* **56**, 1006-1013 (2019).

34   Burchell, T. D. & Snead, L. L. The effect of neutron irradiation damage on the properties of grade NBG-10 graphite. *Journal of Nuclear Materials* **371**, 18-27, doi:10.1016/j.jnucmat.2007.05.021 (2007).

35   Kelly, B. Irradiation behavior of fine-grain graphites. *Fusion technology* **16**, 96-103 (1989).

36   Pitner, A. Irradiation behavior of POCO graphites. *Carbon* **9**, 637-644 (1971).

37   Best, J., Stephen, W. & Wickham, A. Radiolytic graphite oxidation. *Progress in Nuclear Energy* **16**, 127-178 (1985).

38   Babout, L., Mummery, P. M., Marrow, T. J., Tzelepi, A. & Withers, P. J. The effect of thermal oxidation on polycrystalline graphite studied by X-ray tomography. *Carbon* **43**, 765-774, doi:10.1016/j.carbon.2004.11.002 (2005).

39   Labaton, V., Ashton, B., Lind, R. & Tait, J. The effect of variation in pore size on the rate of radiolytic corrosion of graphite by carbon dioxide. *Carbon* **7**, 59-75 (1969).

40   Jones, K. L., Laudone, G. M. & Matthews, G. P. A multi-technique experimental and modelling study of the porous structure of IG-110 and IG-430 nuclear graphite. *Carbon* **128**, 1-11 (2018).

41   Arregui-Mena, J. D. *et al.* Using porous random fields to predict the elastic modulus of unoxidized and oxidized superfine graphite. *Materials & Design* **220**, 110840 (2022).

42   Densham, B. *et al.* in *46th ICFA Advanced Beam Dynamics Workshop on High-Intensity and High-Brightness Hadron Beam, Morschach, Switzerland, October 2010.*

43   Graphite, P. *POCO Graphite manufacturer datasheet*, <https://www.entegris.com/content/dam/shared-product-assets/specialty-shared/datasheet-industrial-graphite-7085.pdf> (2014).

44   Jiang, M. *et al.* Multiple length-scale microstructural characterisation of four grades of fine-grained graphite. *Journal of Nuclear Materials* **550**, 152876 (2021).

45   Dragonfly, 3D visualization and analysis solutions for scientific and industrial data v. 2022.1 (Object Research Systems (ORS) Inc, Montréal (Québec), Canada, 2022).

46   Campbell, A. A. & Was, G. S. Proton irradiation-induced creep of ultra-fine grain graphite. *Carbon* **77**, 993-1010, doi:10.1016/j.carbon.2014.06.016 (2014).

47   Bidhar, S., Simos, N., Senor, D. & Hurh, P. Failure investigation of nuclear grade POCO graphite target in high energy neutrino physics through numerical simulation. *Nuclear Materials and Energy* **24**, 100761 (2020).

48   Hoinkis, E. in *Studies in Surface Science and Catalysis* Vol. 39   193-202 (Elsevier, 1988).

49   Campbell, A. A. *The Mechanism of Proton Irradiation-Induced Creep in Ultra-Fine Grain Graphite* Doctor of Philosophy thesis, University of Michigan, (2014).

50   Arregui-Mena, J. D., Edmondson, P. D., Campbell, A. A. & Katoh, Y. Site specific, high-resolution characterisation of porosity in graphite using FIB-SEM tomography. *Journal of Nuclear Materials* **511**, 164-173 (2018).

51   Saif, T., Lin, Q., Butcher, A. R., Bijeljic, B. & Blunt, M. J. Multi-scale multi-dimensional microstructure imaging of oil shale pyrolysis using X-ray micro-tomography, automated ultra-high resolution SEM, MAPS Mineralogy and FIB-SEM. *Applied energy* **202**, 628-647 (2017).

52   Liu, Y., King, H. E., Van Huis, M. A., Drury, M. R. & Plümper, O. Nano-tomography of porous geological materials using focused ion beam-scanning electron microscopy. *Minerals* **6**, 104 (2016).

53   Arregui-Mena, J. D., Seibert, R. L. & Gerczak, T. J. Characterization of PyC/SiC interfaces with FIB-SEM tomography. *Journal of Nuclear Materials* **545**, 152736 (2021).

54   Badran, A. *et al.* Automated segmentation of computed tomography images of fiber-reinforced composites by deep learning. *Journal of Materials Science* **55**, 16273-16289 (2020).

55   Novikov, A. A., Major, D., Wimmer, M., Lenis, D. & Bühler, K. Deep sequential segmentation of organs in volumetric medical scans. *IEEE transactions on medical imaging* **38**, 1207-1215 (2018).

56   Ronneberger, O., Fischer, P. & Brox, T. in *Medical Image Computing and Computer-Assisted Intervention–MICCAI 2015: 18th International Conference, Munich, Germany, October 5-9, 2015, Proceedings, Part III 18.* 234-241 (Springer).

57   Jégou, S., Drozdzal, M., Vazquez, D., Romero, A. & Bengio, Y. in *Proceedings of the IEEE conference on computer vision and pattern recognition workshops.* 11-19.

58   Pellemoine, F. in *Physics with SPIRAL2 Heavy Ion Beams at GANIL*   (2022).

59   Rudy J.M. Konings, R. E. S. in *Toward the Use of Ion Irradiation to Predict Reactor Irradiation Effects*   (ed Steven J. Zinkle Gary S. Was) 468-484 (Elsevier, 2020).

60   Reynolds, W. & Thrower, P. The flux-level effect in radiation damage in graphite. *Journal of Nuclear Materials* **10**, 209-214 (1963).

61   Bridge, H., Kelly, B. & Nettley, P. Effect of high-flux fast-neutron irradiation on the physical properties of graphite. *Carbon* **2**, 83-93 (1964).

62   Vreeling, J., Wouters, O. & Van der Laan, J. Graphite irradiation testing for HTR technology at the High Flux Reactor in Petten. *Journal of nuclear materials* **381**, 68-75 (2008).

63   Campbell, A. A., Katoh, Y., Snead, M. A. & Takizawa, K. Property changes of G347A graphite due to neutron irradiation. *Carbon* **109**, 860-873, doi:10.1016/j.carbon.2016.08.042 (2016).

64   Selby, D. L., Garrett, D., Lucas, A. & Reeves, M. Scientific upgrades at the high flux isotope reactor at Oak Ridge National Laboratory. (2001).

65   Bell, J. *et al.* Stored energy in the graphite of power-producing reactors. *Philosophical Transactions of the Royal Society of London. Series A, Mathematical and Physical Sciences* **254**, 361-395 (1962).

66   Eason, E. *et al.* The origins and use of the equivalent temperature concept. *Journal of nuclear materials* **381**, 106-113 (2008).

67   Caturla, M. J. *et al.* Multiscale modeling of radiation damage: applications to damage production by GeV proton irradiation of Cu and W, and pulsed irradiation effects in Cu and Fe. *Journal of nuclear materials* **296**, 90-100 (2001).

68   Kmetyk, L., Weertman, J., Green, W. & Sommer, W. Void growth and swelling for cyclic pulsed radiation. *Journal of Nuclear Materials* **98**, 190-205 (1981).

69   Liu, D., Mingard, K., Lord, O. T. & Flewitt, P. On the damage and fracture of nuclear graphite at multiple length-scales. *Journal of Nuclear Materials* **493**, 246-254, doi:10.1016/j.jnucmat.2017.06.021 (2017).

70   Heard, P., Wootton, M., Moskovic, R. & Flewitt, P. Deformation and fracture of irradiated polygranular pile grade A reactor core graphite. *Journal of nuclear materials* **418**, 223-232 (2011).

71   Krishna, R., Jones, A. N., McDermott, L. & Marsden, B. J. Neutron irradiation damage of nuclear graphite studied by high-resolution transmission electron microscopy and Raman spectroscopy. *Journal of Nuclear Materials* **467**, 557-565, doi:10.1016/j.jnucmat.2015.10.027 (2015).

845   72   Heard, P. J., Payne, L., Wootton, M. & Flewitt, P. E. Evaluation of surface deposits on the channel wall of trepanned reactor core graphite samples. *Journal of Nuclear Materials* **445**, 91-97 (2014).

73   Tzelepi, A. *et al.* Studies of irradiation creep on core graphite by thermal annealing. *Journal of Nuclear Materials* **539**, 152309 (2020).

850   74   Zhang, B. *et al.* Characterization of the effects of 3-MeV proton irradiation on fine-grained isotropic nuclear graphite. *Carbon* **77**, 311-318 (2014).

75   Huang, Q. *et al.* Raman spectra and modulus measurement on the cross section of proton-irradiated graphite. *Nuclear Instruments and Methods in Physics Research Section B: Beam Interactions with Materials and Atoms* **412**, 221-226, doi:10.1016/j.nimb.2017.09.004 (2017).

855   76   Kim, E.-S. & Kim, Y.-W. Characterization of 3 MeV H+ irradiation induced defects in nuclear grade graphite. *Solid state communications* **150**, 1633-1636 (2010).

77   Amirkhani, M. A., Asadi Asadabad, M., Hassanzadeh, M. & Mirvakili, S. M. The effects induced by proton irradiation on structural characteristics of nuclear graphite. *Journal of Radioanalytical and Nuclear Chemistry* **321**, 701-709 (2019).

860   78   Hove, J. E. in *Pergamon Press* (eds H. M. Finniston & J. E. Hove) 551-569 (1959).

79   Was, G. S. & Was, G. S. Emulating neutron irradiation effects with ions. *Fundamentals of Radiation Materials Science: Metals and Alloys*, 631-665 (2017).

80   Was, G. *et al.* Emulation of reactor irradiation damage using ion beams. *Scripta Materialia* **88** (2014).

865   81   Was, G. *et al.* Emulation of neutron irradiation effects with protons: validation of principle. *Journal of nuclear materials* **300**, 198-216 (2002).

82   Simos, N. *et al.* Proton irradiated graphite grades for a long baseline neutrino facility experiment. *Physical Review Accelerators and Beams* **20**, doi:10.1103/PhysRevAccelBeams.20.071002 (2017).

870   83   Kelly, B. T. Graphite—the most fascinating nuclear material. *Carbon* **20**, 3-11 (1982).

84   Tanabe, T. Radiation damage of graphite-degradation of material parameters and defect structures. *Physica Scripta* **1996**, 7 (1996).

85   Heggie, M., Suarez-Martinez, I., Davidson, C. & Haffenden, G. Buckle, ruck and tuck: A proposed new model for the response of graphite to neutron irradiation. *Journal of nuclear* 875   *materials* **413**, 150-155 (2011).

86   Johns, S. *et al.* Experimental evidence for 'buckle, ruck and tuck'in neutron irradiated graphite. *Carbon* **159**, 119-121 (2020).

87   Liu, D. *et al.* A macro-scale ruck and tuck mechanism for deformation in ion-irradiated polycrystalline graphite. *Carbon* **173**, 215-231 (2021).

880   88   Kelly, B. T., Martin, W. H. & Nettley, P. Dimensional changes in pyrolytic graphite under fast-neutron irradiation. *Philosophical Transactions of the Royal Society of London. Series A, Mathematical and Physical Sciences* **260**, 37-49 (1966).

89   Kelly, B., Martin, W., Price, A. & Bland, J. The mechanism of dimensional changes in the crystals of graphites and carbons under fast neutron irradiation. *Philosophical Magazine* **14**, 343-356 885   (1966).

90   Jiang, M., Ammigan, K., Lolov, G., Pellemoine, F. & Liu, D. A novel method for quantifying irradiation damage in nuclear graphite using Raman spectroscopy. *Carbon*, 118181 (2023).

91   Karthik, C., Kane, J., Butt, D. P., Windes, W. & Ubic, R. In situ transmission electron microscopy of electron-beam induced damage process in nuclear grade graphite. *Journal of Nuclear* 890   *Materials* **412**, 321-326 (2011).

92   Shen, K., Zhang, X., Yu, S. & Kang, F. Characterization of heterogeneity in NBG-18 nuclear graphite microstructure by correlative analysis of optical texture and focused ion beam transmission electron microscopy observations. *Carbon* **189**, 604-616 (2022).

93   Johns, S. *et al.* Fullerene-like defects in high-temperature neutron-irradiated nuclear graphite. 895   *Carbon* **166**, 113-122 (2020).

94   Karthik, C., Kane, J., Butt, D. P., Windes, W. E. & Ubic, R. Neutron irradiation induced microstructural changes in NBG-18 and IG-110 nuclear graphites. *Carbon* **86**, 124-131 (2015).

95   Casella, A., Senor, D., Edwards, D., Schemer-Kohrn, A. & Asner, D. Post-Irradiation Examination of Graphite from the NuMI NT-02 Target. (Pacific Northwest National Laboratory, 2016).

96   Contescu, C. I. *et al.* Development of mesopores in superfine grain graphite neutron-irradiated at high fluence. *Carbon* **141**, 663-675 (2019).

97   Campbell, A. A. & Katoh, Y. Report on Effects of Irradiation on Material IG-110-Prepared for Toyo Tanso Co., Ltd. (Oak Ridge National Lab.(ORNL), Oak Ridge, TN (United States), 2017).

98   Ishiyama, S., Burchell, T., Strizak, J. & Eto, M. The effect of high fluence neutron irradiation on the properties of a fine-grained isotropic nuclear graphite. *Journal of Nuclear Materials* **230**, 1-7 (1996).

99   Heijna, M. C. R., de Groot, S. & Vreeling, J. A. Comparison of irradiation behaviour of HTR graphite grades. *Journal of Nuclear Materials* **492**, 148-156, doi:10.1016/j.jnucmat.2017.05.012 (2017).

100   Kennedy, C. & Woodruff, E. Irradiation Effects on the Physical Properties of Grade TSX Graphite. *Westinghouse Hanford Company, Richland, Washington* (1989).

101   Marsden, B. J. & Hall, G. N. Graphite in gas-cooled reactors. *Reference Module in Materials Science and Materials Engineering* **14**, 357-421 (2020).

102   Platonov, P. A. *et al.* Properties of neutron irradiated carbon-based materials for fusion reactor application. *Plasma Devices and Operations* **3**, 79-92, doi:10.1080/10519999408201804 (1994).

103   Campbell, A. A. & Was, G. S. In situ proton irradiation-induced creep at very high temperature. *Journal of nuclear materials* **433**, 86-94 (2013).

104   Snead, L. L., Contescu, C. I., Byun, T. S. & Porter, W. Thermophysical property and pore structure evolution in stressed and non-stressed neutron irradiated IG-110 nuclear graphite. *Journal of Nuclear Materials* **476**, 102-109 (2016).

105   Oku, T., Fujisaki, K. & Eto, M. Irradiation creep properties of a near-isotropic graphite. *Journal of Nuclear Materials* **152**, 225-234 (1988).

106   Brooking, M., Reed, J. & Davies, M. Project ACCENT: graphite irradiation-induced creep in a materials test reactor. (2015).

107   van Staveren, T., Davies, M., Knol, S. & de Koning, A. Design, construction and operation of a graphite irradiation creep facility. *Nuclear Engineering and Design* **364**, 110588 (2020).

108   Haag, G. Properties of ATR-2E graphite and property changes due to fast neutron irradiation. (2005).

109   Windes, W., Burchell, T. & Davenport, M. The advanced reactor technologies (art) graphite R&D program. *Nuclear Engineering and Design* **362**, 110586 (2020).

110   Bacon, D. & Rao, A. The structure of graphite bombarded with light, gaseous ions. *Journal of Nuclear Materials* **91**, 178-188 (1980).

111   Chernikov, V., Kesternich, W. & Ullmaier, H. Radiation effects and gas cavities in pyrolytic graphite implanted with helium ions. *Journal of nuclear materials* **227**, 157-169 (1996).

112   Sone, K., Abe, T., Obara, K., Yamada, R. & Ohtsuka, H. Graphite surface erosion by 100 keV helium and hydrogen bombardment. *Journal of Nuclear Materials* **71**, 82-88 (1977).

113   Niwase, K. & Tanabe, T. Defect structure and amorphization of graphite irradiated by D+ and He+. *Materials transactions, JIM* **34**, 1111-1121 (1993).

114   Kelly, A. & Mayer, R. The influence of boron on the clustering of radiation damage in graphite: I. Electron microscopic observations. *Philosophical Magazine* **19**, 701-719 (1969).

115   Ammigam, K. in *Workshop on Radiation Damage in Accelerator Materials and the Potential Use of the Versatile Test Reactor for the Study of Accelerator Materials*   (2022).